Acta Materialia 250 (2023) 118856

Contents lists available at ScienceDirect

Acta Materialia

journal homepage: www.elsevier.com/locate/actamat

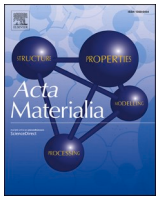

From high-entropy alloys to high-entropy ceramics: The radiation-resistant highly concentrated refractory carbide (CrNbTaTiW)C

Matheus A. Tunes [a,*], Stefan Fritze [b,*], Barbara Osinger [b], Patrick Willenshofer [g], Andrew M. Alvarado [d,e,f], Enrique Martinez [d,e,f], Ashok S. Menon [b], Petter Ström [c], Graeme Greaves [h], Erik Lewin [b], Ulf Jansson [b], Stefan Pogatscher [g], Tarik A. Saleh [a], Vladimir M. Vishnyakov [h], Osman El-Atwani [a]

[a] Materials Science and Technology Division, Los Alamos National Laboratory, Los Alamos, NM 87545, United States
[b] Department of Chemistry, Angstrom Laboratory, Uppsala University, Uppsala SE-751 21, Sweden
[c] Department of Physics and Astronomy, Applied Nuclear Physics, Uppsala University, Uppsala SE-751 21, Sweden
[d] Theoretical Division, Los Alamos National Laboratory, Los Alamos, NM 87545, United States
[e] Department of Materials Science and Engineering, Clemson University, Clemson, SC 29623, United States
[f] Department of Mechanical Engineering, Clemson University, Clemson, SC 29623, United States
[g] Chair of Non-Ferrous Metallurgy, Montanuniversität Leoben 8700, Austria
[h] School of Computing and Engineering, University of Huddersfield, Huddersfield HD1 3DH, United Kingdom

ARTICLE INFO

Keywords:
High-entropy ceramics
High-entropy alloys
Nanocrystalline materials
Radiation damage
Extreme environments

ABSTRACT

High-entropy materials represent the state-of-the-art on the alloy design strategy for future applications in extreme environments. Recent data indicates that high-entropy alloys (HEAs) exhibit outstanding radiation resistance in face of existing diluted alloy counterparts due to suppressed damage formation and evolution. An extension of the HEA concept is presented in this paper towards the synthesis and characterization of novel high-entropy ceramics as emergent materials for application in environments where energetic particle irradiation is a major concern. A novel carbide within the quinary refractory system CrNbTaTiW has been synthesized using magnetron-sputtering. The material exhibited nanocrystalline grains, single-phase crystal structure and C content around 50 at.%. Heavy-ion irradiation with in-situ Transmission Electron Microscopy was used to assess the irradiation response of the new high-entropy carbide (HEC) at 573 K and a comparison with the HEA within the system is made. No displacement damage effects appear within the microstructures of both HEA and HEC up to a dose of 10 displacements-per-atom. Surprisingly, the HEC has not amorphized under the investigated conditions. Xe was implanted in both materials and bubbles nucleated, but smaller sizes compared with conventional nuclear materials shedding light they are potential candidates for use in nuclear energy.

1. Introduction

The need for materials able to withstand extreme environments, for example faced in nuclear reactors, warrants the investigation of new alloys and related compounds. A great leap forward in alloy design and metallurgy was marked by the development of high-entropy alloys (HEAs), first introduced by Yeh et al. and Cantor et al in 2004 [1–4]. HEAs are formed with multiple principal elements in highly-concentrated compositions, as opposed to the conventional alloy design methodology focused on terminal solid solutions, where a single element serves as basis for alloying with other elements in small quantities [1,2,5–9]. The extensive alloying in these multicomponent metallic systems results in the stabilization of a random single-phase solid solution, typically body centred cubic (BCC) or cubic close-packed (CCP) structure. The increased configurational entropy, characteristic of systems with constituents in (or closer to) equimolar composition, is believed to play a major role in the single-phase stabilization, although recent research has indicated these hypotheses are pending clarification [10–18].

HEAs have been shown to outperform existing materials for several applications in technologically relevant areas like mechanical performance and extreme environments, such as nuclear fission & fusion

* Corresponding authors.
E-mail addresses: m.a.tunes@physics.org (M.A. Tunes), ist.stefanf@gmail.com (S. Fritze).

https://doi.org/10.1016/j.actamat.2023.118856
Received 25 January 2023; Received in revised form 9 March 2023; Accepted 10 March 2023
Available online 12 March 2023

reactors, thus making them potential new functional materials [19–31]. On the latter aspect on materials for extreme environments – the focus of this present work – the current demands are to design materials that may outperform existing solutions by increasing their resistance to exposure at low and high temperatures and to the deleterious effect of energetic particle irradiation commonly found in nuclear reactors and in the solar system [32–37].

Over time the high-entropy concept has expanded to include high-entropy ceramics and led to the development of high-entropy carbides and oxides (HECs and HEOs). HECs may harness all the potential of ceramics which, compared to metallic alloys, can exhibit significantly higher hardness, high temperature stability and corrosion resistance [38–41]. Nonetheless, high-entropy ceramics are much less studied in this regard, compared with HEAs.

Earlier studies on the radiation resistance of HECs were carried out by Wang and Yan et al and Zhu et al on SPS bulk materials [42,43]. The former investigating the response of (Zr0.25Ta0.25Nb0.25Ti0.25)C to 3 MeV Zr ions up to 20 displacements-per-atom (dpa), while the latter investigated the damage evolution under self-ion irradiation in (WTiVNbTa)C5, using 1 MeV C ions up to 22 dpa [42,43]. These authors have reported that void formation, radiation-induced segregation (RIS) and amorphization have not occurred within the dose and temperature ranges studied, thus serving as motivation for new studies on the radiation resistance of HECs. Nevertheless, these authors used TEM to confirm the formation of irradiation-induced defect clusters in a form of perfect dislocation loops and faulted Frank loops and their suppressed growth was attributed to severe lattice distortion hindering dislocation movement: a characteristic constitutive hypothesis of HEA systems [44]. To the authors knowledge, even fewer studies have been published on the irradiation behavior of HEC coatings and thin films, despite the clear benefits of surface modification such as ease of synthesis and the possibility to screen a wide compositional space, as well as cost and weight-effectiveness.

In this work we report the characterization and investigation of a HEC and a HEA, synthesized via non-reactive magnetron-sputtering, on application relevant steel substrates. The radiation resistance of a nanocrystalline refractory HEC is herein assessed using heavy ion irradiation with in-situ transmission electron microscopy (TEM) with the focus of detecting possible morphological changes such as grain growth and/or phase transformations, local chemical instabilities like RIS and/or precipitation (RIP) and inert gas bubbles formation. The HEC was chosen to be in a nanocrystalline form to investigate the effect of grain boundaries in the response of HECs to extreme environments.

The (CrNbTaTiW)C system was chosen since a similar version of this refractory system, consisting of WTaVCr, was reported to have outstanding radiation resistance within the context of nuclear fusion reactors [45]. Additionally, superior corrosion and mechanical resistance, compared with conventional binary carbides, have been demonstrated for (CrNbTaTiW)C coatings in a previous study [46]. The microstructure and properties of quinary CrNbTaTiW HEA thin films have also been investigated previously [47]. By comparing the performance of HEC and HEA, the effect of carbon is studied and whether the HEC can present suitable levels of radiation resistance to be useful as functional materials for applications in extreme environments.

2. Experimental methods

2.1. Synthesis via magnetron sputtering

The materials were synthesized via non-reactive DC-magnetron sputtering from Nb, pre-alloyed Ti/Cr (composition ratio 1:1), segmented Ta/W (composition ratio 1:1) and C circular sputtering targets (diameter 5 cm) with purity level of 99.9%. The chamber base pressure was below 3.8×10^{-7} Pa. Mirror-like polished austenitic stainless-steel grade AISI-316L was used as substrates for deposition and they were placed on a rotating holder and pre-heated to 573 K for 1 h to minimize the risk of temperature gradients. During the deposition the working gas pressure was kept constant at 0.6 Pa with an Ar gas flow rate of 42 sccm. The electric currents of the magnetrons were adjusted during co-sputtering to obtain the desired compositions. The materials present in this study were synthesized as part of a larger study of refractory high entropy alloys [46,47].

2.2. Elastic/Rutherford backscattering spectrometry and particle-induced X-ray emission

The chemical compositions of the films were estimated by means of ion-beam based analytical techniques at the Tandem Laboratory at Uppsala University. Rutherford Backscattering Spectrometry (RBS) measurements were performed using 2 MeV $^{4}He^{+}$ as primary ions, and Elastic Backscattering Spectroscopy (EBS) measurements were carried out using the elastic $^{12}C(4He,4He)^{12}C$ resonance with a 4.45 MeV He^{2+} beam probing C at the resonance energy of 4.26 MeV near a sample depth of approximately 80 nm [48,49]. All measurements were performed with the incident beam at 5° with respect to the normal surface and the backscattering angle was 170°. The samples were wiggled within a 2° angle interval to avoid possible channeling effects. The data analysis was performed using the SIMNRA software package and the cross sections obtained from SigmaCalc were used to fit the C peak [49]. Particle induced X-ray emission (PIXE) measurements were performed simultaneously with the EBS/RBS measurement. The PIXE detector was mounted at 135° and further details about the PIXE setup are given elsewhere [50]. The PIXE data was analyzed using with the GUPIX software [51].

Time-of-Flight Energy Elastic Recoil Detection Analysis (ToF-E-ERDA) measurements were carried out using 36 MeV $^{127}I^{8+}$ (iodine) as the projectile species. The scattered ions were detected at an angle of 45° with respect to the primary beam with the incidence and exit angle of beam and detected particles set to 22.5° with respect to the sample surface [52]. The ERDA data was analyzed using the Potku software [53]. To extract the C and O fractions an integration depth of 0 to 225 nm was used, consequently including the surface oxide layer.

All IBA measurements were carried out on Si substrates that were placed next to the AISI-316L substrates during deposition, to avoid overlap of the Cr signals from the film and the substrates

2.3. X-ray diffraction characterization

A Philips MRD X'Pert diffractometer with Cu Kα radiation was used to perform grazing incidence X-ray diffraction (GI-XRD) measurements with an incident angle of 2°. The diffractometer was operated in a parallel beam geometry using a Göbel mirror on the primary side and parallel plate collimator with a 0.27° divergence on the secondary side. Pawley refinement of the cubic unit cells against the XRD data was carried out using the Topas Academic (V6) software [54,55].

2.4. Focused Ion beam

A FEI Strata DB235 scanning electron microscope with coupled focused ion beam (SEM-FIB) was used to prepare cross-sectional electron-transparent specimens of the synthesized materials for transmission electron microscopy (TEM) characterization and heavy ion irradiation with in-situ TEM. The lamellas were attached to either Cu or Mo lift-out grid and subsequently thinned to electron transparency with a final polishing step using a 5 kV Ga^{+} beam following methodology from literature [56].

2.5. Transmission electron microscopy

Pre- and post-irradiation characterization was performed using a FEI Talos F200X STEM operating a field emission gun with the energy set to 200 keV. This STEM was mainly used for microstructural analytical

investigations via the Super-X Energy Dispersive X-ray (EDX) spectroscopy technique, High-Angle Annular Dark-Field (HAADF) and Bright-Field STEM (BF-STEM). Prior to the electron-microscopy investigations using a FEI Talos, all the TEM lamellae were subjected to plasma cleaning in an Ar atmosphere for 20 min, which was found sufficient to prevent C (or any contaminants) uptake during prolonged STEM-EDX experiments. For elemental quantification using the collected STEM-EDX data, a multi-polynomial model with Brown-Powell cross sections and sloped background was used for spectral fitting assuming that the thicknesses of the samples were approximately 100 nm. The densities of both HEC and HEA were set to 13.5 and 17.1 g cm^{-3}, respectively. Bright-Field TEM (BFTEM), Dark-Field TEM (DFTEM) and Selected Area Electron Diffraction (SAED) techniques were performed in a FEI Tecnai F30 TEM operating a Schottky FEG at 300 keV also for the pre- and post-irradiated specimens. Fresnel contrast was used for the identification of nanometer-sized Xe bubbles. DFTEM micrographs were digitally colored using the lookup tables within the ImageJ software for better visualization and grain-size measurement [57].

2.6. In situ TEM with heavy ion irradiation

The electron-transparent samples produced in the SEM-FIB were subjected to heavy ion irradiations in situ in a Hitachi H-9500 TEM operating at 300 keV at the MIAMI-2 facility in the University of Huddersfield [58]. The accelerator coupled with the TEM is a 350 kV ion source from National Electrostatics Corporation and a 300 keV Xe^{+} ion beam with a flux of 6.2×10^{12} ions cm^{-2} s^{-1} was used to irradiate the specimens up to a fluence of 3.7×10^{15} ions cm^{-2}. All specimens were subjected to irradiations at 573 K to emulate the thermal environment commonly found in light-water reactors. SRIM-2013Pro was used to convert fluence-to-dpa following a slightly modified version of the method proposed by Stoller et al. [59] Although Stoller's method has been recently revisited in the specific case of highly concentrated multicomponent systems [20], which suggested the use of the "full damage cascades" mode of calculation instead of "quick calculation of damage" mode, the earlier method is still widely used to calculate the equivalent nuclear reactor dose in dpa for ion beams.

Using the "quick calculation of damage" mode of calculation within the SRIM-2013Pro, an assumed thickness of around 100 nm and 40 eV [59,60] as an average displacement energy for all the metal constituents and 28 eV for C, SRIM-2013Pro estimates an average of 2066 and 2102 displacements-per-ion collision for the HEC and the HEA, respectively (from the VACANCY.txt file). For these calculations, the theoretical density of both HEC and HEA were used: 13.5 and 17.1 g cm^{-3}, respectively, and the measured elemental compositions were used as presented in Table 1. Under these conditions, the maximum fluence of our experiments corresponds to approximately 9.0 and 12.6 dpa for both HEC and HEA. Throughout this paper, for clarification and comparison purposes, we reasonably approximate the total dose for both materials to 10 dpa as both materials were subjected to the same dose rate (flux) and fluence.

Table 1
Elemental composition estimated via EBS/PIXE[a] analysis of the as-deposited designed materials. The C concentration in the HEA film and the O concentration in both films was determined by ToF-E- ERDA measurements.

Material	Elemental Composition [at.%]						
	Cr	Nb	Ta	Ti	W	C	O
HEA	1.8	9.0	46.0	1.1	42.1	<1	< 1
HEC	3.1	5.9	21.7	3.3	21.7	44.3	< 1

[a] A 2 MeV He^{+} ion beam was used for the HEA and a 4.45 MeV He^{2+} ion beam was used for the HEC.

2.7. Density functional theory computation

DFT calculations are performed using density functional software package VASP [61,62]. For the exchange and correlation, we use a generalized gradient approximation of the Perdew-Burke-Ernzerhof form [63] (GGA-PBE), and projector augmented wave pseudopotentials. Both the semi-core electrons and magnetic contributions are not included in this study. We find the contribution from both do not significantly affect the calculations. The convergence criteria for energy and forces are set to 10^{-5} eV and 10^{-3} eV Å^{-1} respectively. The Monkhorst-Pack mesh [64] spacing is such that it corresponds to a $14 \times 14 \times 14$ k-point mesh of a two-atom body centered cubic (BCC) cell and a $20 \times 20 \times 7$ k-point mesh of a two-atom hexagonal close pack (HCP) cell, that was used to compute reference energies. The plane-wave cutoff energy used was 350 eV. We have generated 20 random solution configurations of $4 \times 4 \times 4$ body-centered cubic supercell structures for an HEA with component concentrations of 3.1Cr, 11.7Nb, 40.6Ta, 3.1Ti, and 41.4W(in at.%). In addition, and similarly for the HEC, we have generated 30 random solution configurations of $3 \times 3 \times 3$ RS cubic supercell structures ceramic with component concentrations of 3.3% Cr, 4.3Nb, 19.2Ta, 3.5Ti, 19.5W, and 50C (in at.%) on the cation sites. In the rock-salt (RS) structure W, Ta, Nb, Ti, and Cr share the anion sites. Each of those atoms are surrounded by C atoms while C atoms are surrounded by the anion site atoms. These configurations have been minimized in energy at zero temperature and pressure, relaxed in volume, and computed the formation energy per atom.

$$E_f = \frac{E_{DFT} - \sum_{m=1}^{n} c_m E_m^{ref}}{N} \quad (1)$$

where E_{DFT} is the energy of system as calculated ab initio, N is the total number of atoms in the supercell, n is number of components in the alloy, and E_m^{ref} and c_m are the reference energy and number of atom type m. The reference energies, E_m^{ref} are −9.511, −10.047, −11.862, −7.762, −13.015, −5.299 eV for Cr, Nb, Ta, Ti, W, and C, respectively. The reference energy for both Ti and C have been computed in an HCP lattice and Cr, Nb, Ta, and W in a BCC lattice.

For these structures we have introduced a vacancy on the sites for W and Ta for BCC structures and W, Ta, and C for the RS structures on 20 random configurations. This equates to a total of 40 configurations in BCC and 60 configurations in RS each with a single vacancy. These structures have also been relaxed at zero pressure and temperature and vacancy formation energy computed.

$$E_f^{vac} = E_{DFT}^{vac} - E_{DFT} + E_m^{ref} \quad (2)$$

where E_{DFT}^{vac} is the energy of the system with a single vacancy as computed ab initio. The reference energy E_m^{ref} is of the atom of type m that is removed.

3. Results

3.1. Synthesis and characterization

The composition of the materials, synthesized via non-reactive DC magnetron sputtering, was determined using Ion Beam Analysis (IBA) methods. Namely Time-of-Flight Energy elastic recoil detection analysis (ToF-E- ERDA), Elastic Backscattering Spectrometry (EBS and Particle-Induced X-ray Emission (PIXE). In addition, grazing incidence X-ray Diffraction (GI-XRD) and Transmission Electron Microscopy (TEM) were used to assess the materials' crystallography and microstructural morphology in their pristine forms.

In Table 1 we present the result of the chemical composition analysis obtained from the different IBA-methods. The experimental EBS spectra of the HEC and the HEA films (black solid dots) are shown along with a fit obtained by SIMNRA (green solid line) in Fig. 1A and C. The EBS fits

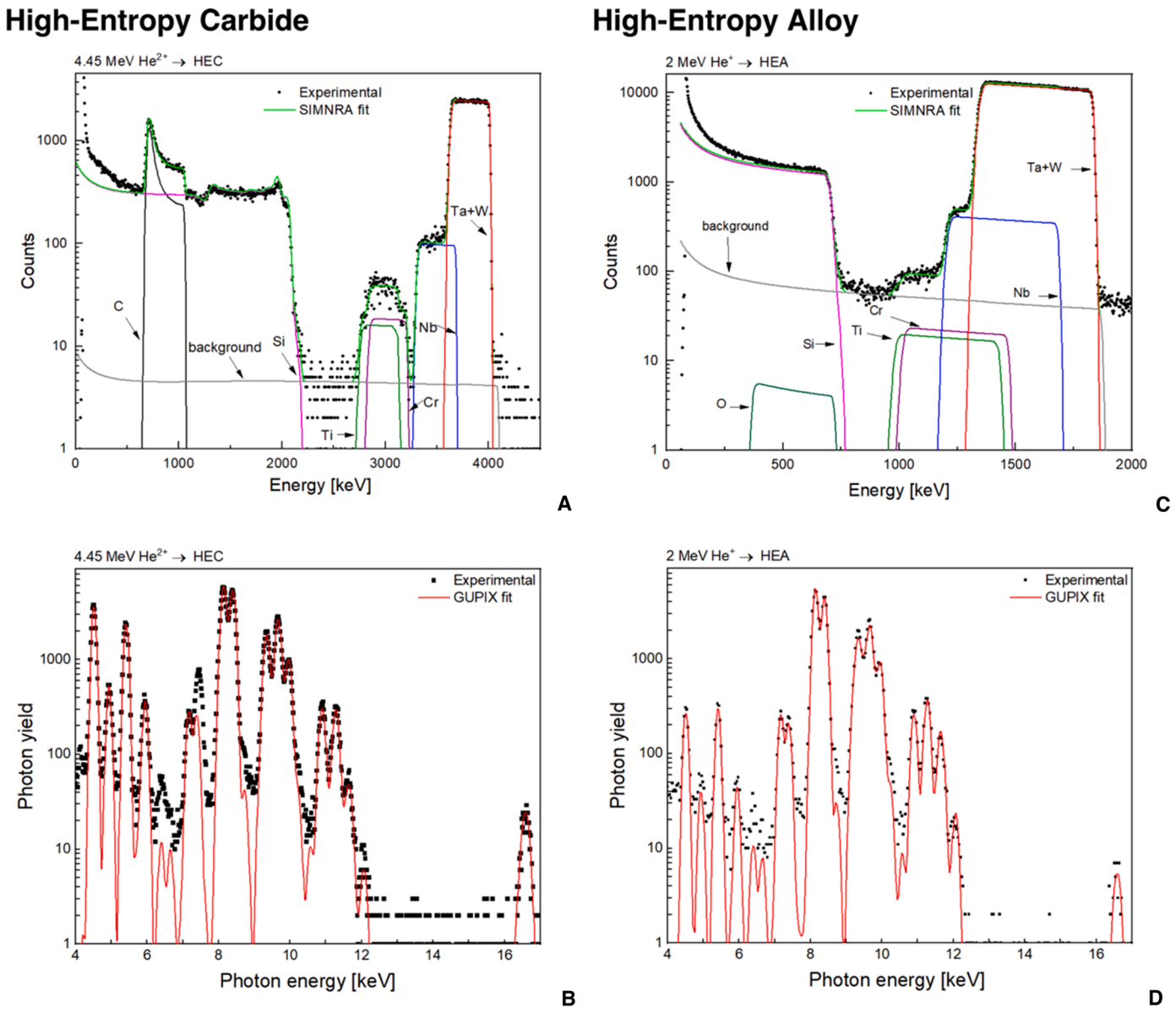

Fig. 1. Ion beam analysis of the designed materials in the as-deposited state. EBS/RBS spectra and PIXE fits obtained with the as-deposited HEC (A and B) and HEA (C and D) specimens, respectively. The fit to the C peak, using cross sections as obtained with SigmaCalc [49] in SIMNRA [94] indicates that this element is incorporated within the HEC solid solution with a molar amount similar to the combined amount of the latter elements. The PIXE fits allowed the estimation of elemental ratios of Ti/Cr and Ta/W. The elemental composition was determined by a combination of EBS/RBS and PIXE Table 1. The photon lines used to estimate the compositions are shown in Table 2 for clarification.

are based on the boundary conditions of known relative Ti/Cr and Ta/W ratios obtained from PIXE (see Fig. 1B and D). The Ti/Cr ratio was determined by means of the K line series and the Ta/W ratio was determined by an analysis of all detectible L-lines. A detailed overview of the detected X-ray energy lines used in this work is presented in Table 2.

Four distinct plateaus are observed for the HEC films (Fig. 1A) while three distinct plateaus are observed in the case of the HEA film (Fig. 1C). The broad plateau at high energies in the range from 3700 to 4050 keV in the case of the HEC film and in the range from 1350 to 1825 keV in the case of the HEA film corresponds to the Ta+W signal. The relative narrow plateau at energies in the range from 3400 to 3600 keV in Fig. 1A and in the range from 1225 to 1290 keV in Fig. 1C corresponds to Nb. Similarly, the plateau at energies in the range from 2750 to 3350 keV for the HEC film and in the range from 1020 to 1160 keV for the HEA film corresponds to Ti+Cr. The C signal is detected at energies around 750–1150 keV for the HEC film. Additional ToF-E- ERDA measurements

Table 2
Photon energy lines used to determine the elemental ratios used to estimate the elemental composition of the deposited films.

Element	Photon energy [keV]						
Ti	Kα	Kβ					
	4.51	4.93					
Cr	Kα	Kβ					
	5.41	5.95					
Nb	Kα						
	16.58						
Ta	L_l	$L\alpha_1$	$L\alpha_2$	$L\beta_1$	$L\beta_2$	$L\gamma_1$	$L\gamma_3$
	7.17	8.15	8.09	9.35	9.65	10.89	11.28
W	L_l	$L\alpha_1$	$L\alpha_2$	$L\beta_1$	$L\beta_2$	$L\gamma_1$	$L\gamma_3$
	7.39	8.40	8.34	9.67	9.96	11.28	11.68

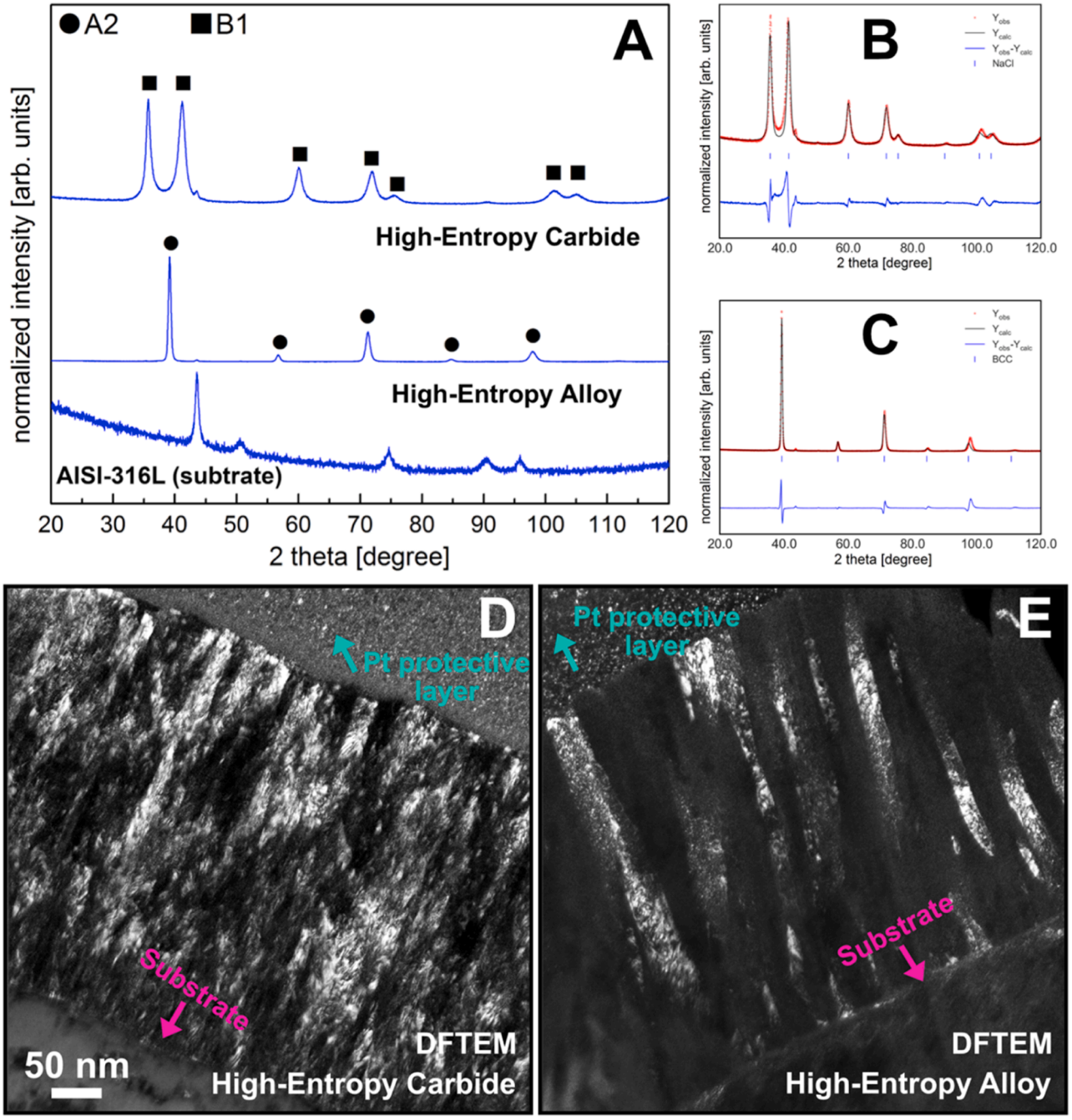

Fig. 2. Crystallographic analysis and microstructural morphology of the designed materials in the as-deposited state. The plot in figure A shows the GI diffractograms for the HEC, HEA and the AISI-316L (substrate). The Pawley refinement analysis in B and C indicated that the HEC has a B1 (NaCl) crystal structure while the HEA is of a A2 (BCC) crystal structure. In the plots B (for the HEC) and C (for the HEA), the black curves represent the simulated patterns, the red curve the observed data and the blue curve denotes the difference between the observed and simulated curves. Peak positions of the used structure models are marked by blue vertical bars below the simulated/observed curves. The calculated lattice parameters are shown in Table 2. The DFTEM micrographs in D and E show the microstructural morphology of the pristine HEC and the HEA, respectively, at the nanoscale. The HEC exhibits an equiaxed-like nanograin microstructure with a trend for a columnar arrangement, while the HEA has pure nanograin-sized columnar-like microstructure. Note: the scale bar in D also applies to E.

show that C is only present in the HEC film and that the O impurity level is below 1 at.% in the bulk of both films (see supplementary information Fig. 1) and that the HEA film contains C impurities which are below 1 at.%. It is worth noting that the poor fit to the line close to 7.5 keV might be attributed to Ni contamination in the sample on the order of 0.1 at.%. However, we do not exclude that a fraction of the beam may have grazed or scattered to the stainless steel out of which the experiment chamber is constructed, thus producing a faint Ni signal.

Fig. 2A shows the Grazing-Incidence XRD (GI-XRD) diffractograms of

Table 3
Lattice parameters estimated from the GI-XRD analysis on the as-deposited designed materials.

Sample	Crystal Structure	*a* [Å]	*Rwp*	*Gof*
HEC	B1 (NaCl)	4.358440(354)	17.76	4.91
HEA	A2 (BCC)	3.243593(117)	24.34	6.46

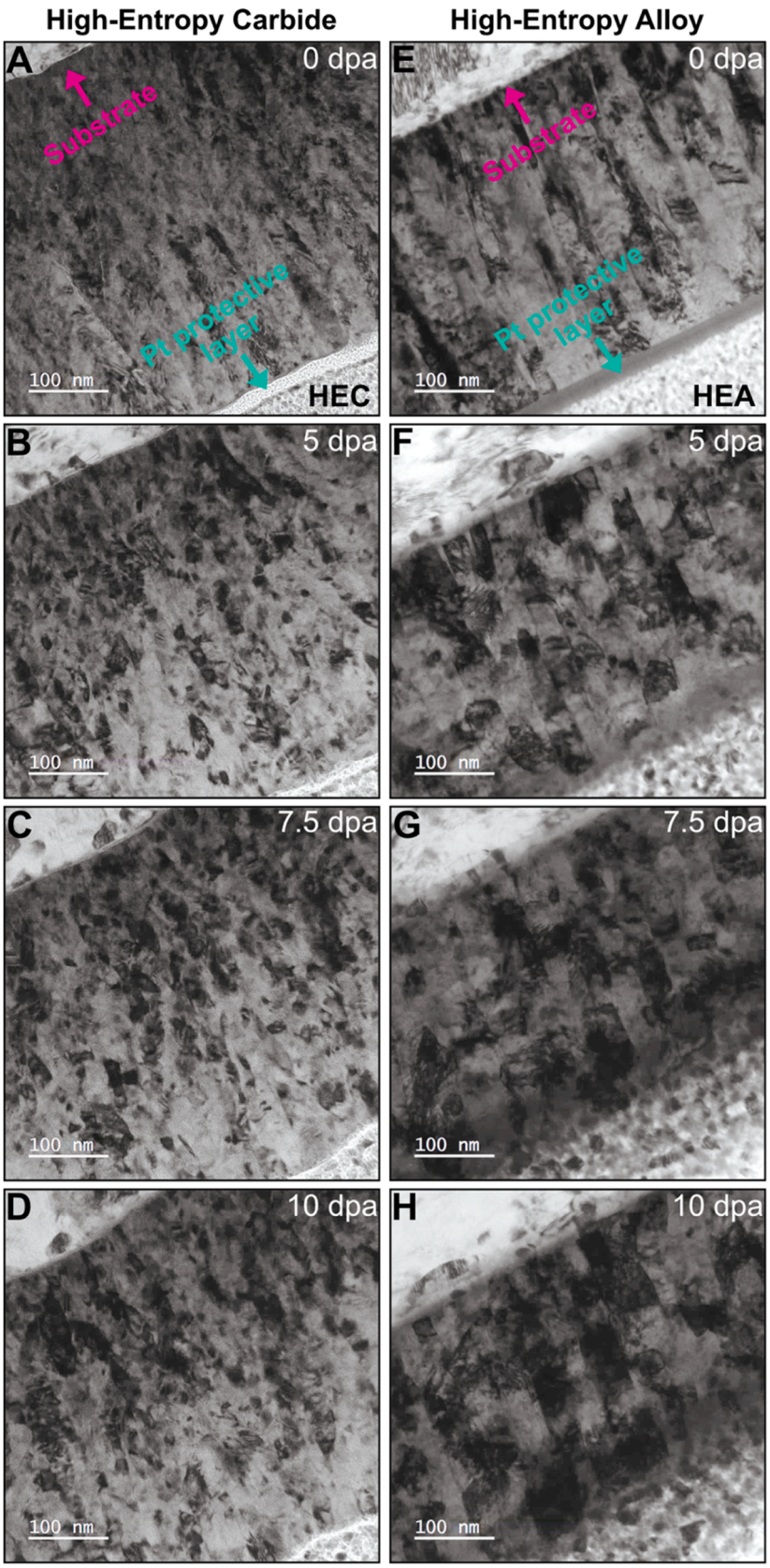

Fig. 3. Microstructural evolution under heavy ion irradiation with in situ TEM. The BFTEM micrographs from A to D and from E to H show the microstructural evolution of the HEC and the HEA under irradiation, respectively, up to a dose of 10 dpa. Note: In situ TEM heavy ion irradiation videos are available in the online version of the article (see Appendix. Supplementary materials).

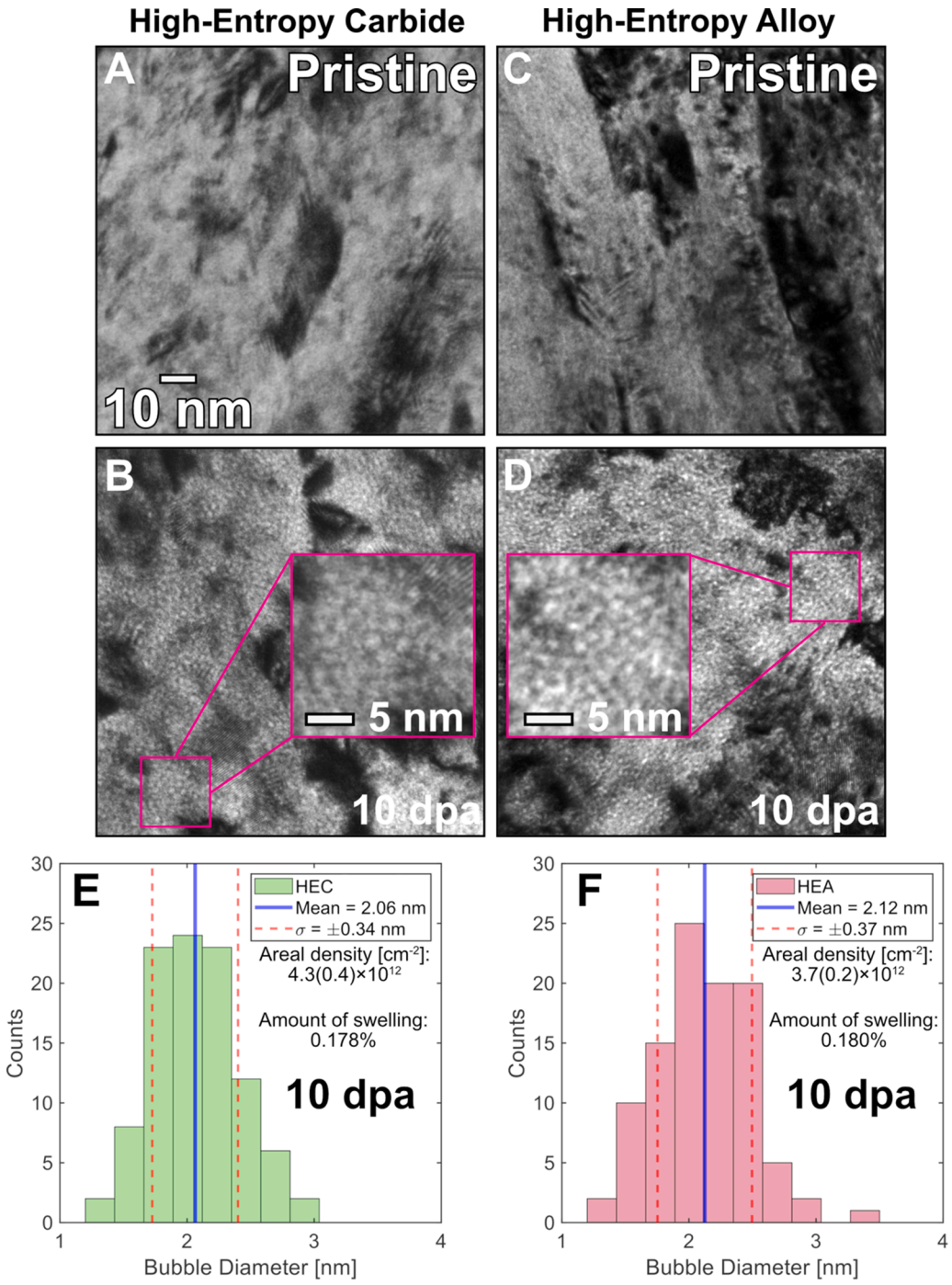

Fig. 4. Xe retention after irradiation. The BFTEM micrographs A and C show the microstructure of both designed materials as-deposited. The under-focused BFTEM micrographs in B and D show Xe bubbles within the microstructures at 10 dpa. The histograms in E and F quantify the average size of the observed Xe bubbles after 10 dpa in the HEC and HEA, respectively. Note: the scale bar in A applies to all micrographs in the figure. The defocus applied was –2100 nm for all the BFTEM micrographs.

the HEC, HEA and the AISI-316L substrate. The HEC diffraction pattern can be fitted with a B1 (NaCl type) structure, and all peaks of the HEA film can be indexed with an A2 (BCC) structure. Pawley refinements (see Fig. 2B and C) were performed to estimate lattice parameters which are presented in Table 3. The additional peaks in the HEC and HEA diffractograms originate from the AISI-316L substrate. Typical morphology of the HEC and HEA films as-deposited is shown in the Dark-Field TEM micrographs in Fig. 2d and e, respectively. The HEC film presents round-shape equiaxed grains arranged in a columnar-like aspect while the HEA film exhibits a typical microstructure with pure columnar grains. The average grain-size was measured using the DFTEM micrographs to be 9.8 ± 0.9 and 27.2 ± 2.4 nm for the HEC and HEA, respectively, therefore both materials are of nanocrystalline nature. We would like to emphasize that the residual differences in the refinements could be explained by crystallographic strain, which can stem from residual compressive stress typical for thin films synthesized by magnetron sputtering [65–67].

3.2. *Heavy ion irradiation with in situ TEM*

The real-time microstructural evolution of both HEC and HEA films under heavy-ion irradiation at 573 K was monitored in situ in a Hitachi H-9500 TEM. Fig. 3A–D shows the microstructure of the HEC under Bright-Field TEM (BFTEM) condition from its pristine state (Fig. 3A) up to a dose of 10 dpa (Fig. 3D). Under BFTEM conditions, it is possible to note a discrete grain growth in the HEC film. Similarly, Fig. 3E–H shows the microstructure of the HEA under BFTEM from its pristine state (Fig. 3E) up to a dose of 10 dpa (Fig. 3H) where the grain growth was

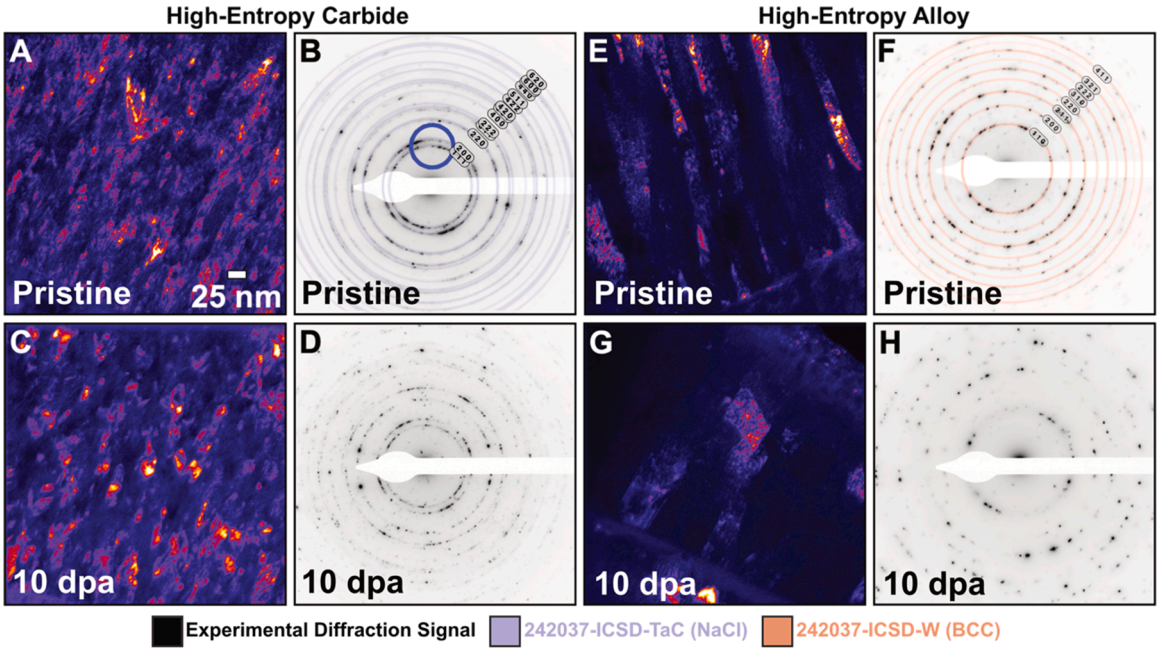

Fig. 5. Morphological modifications after irradiation. The colored DFTEM micrographs in A and C and the SAED patterns in B and D show the microstructure of the HEC and its respective diffraction patterns before and after irradiation, respectively. The average grain size before and after irradiation for the HEC was estimated to be 9.8 ± 0.9 and 14.9 ± 0.8 nm after 10 dpa. The colored DFTEM micrographs in E and G and the SAED patterns in F and H exhibit the microstructure of the HEA before and after irradiation, respectively. For the HEA case, the average grain size before and after 10 dpa was 27.2 ± 2.4 and 60.6 ± 4.1 nm. Note 1: the scale bar in A also applies to C, E and G. Note 2: the SAED patterns in B and F were indexed as shown with data available in the ICSD database [95,96].

more pronounced when compared with the HEC film. Under the observation conditions during the heavy-ion irradiation within in situ TEM, apart from the discrete grain growth, no significant alterations were observed, which motivates a further and detailed post-irradiation characterization.

3.3. Post-irradiation characterization

Multiple electron-microscopy techniques were used to investigate the radiation effects on both HEC and HEA films. These are Fresnel contrast BFTEM, DFTEM and detailed Scanning Transmission Electron Microscopy (STEM) with Energy Dispersive X-ray (EDX) spectroscopy. The results of the post-irradiation characterization are shown in this subsection.

3.3.1. Inert gas bubbles formation

Collected BFTEM micrographs before and after irradiation up to 10 dpa are shown in Fig. 4A–D. After irradiation, transgranular Xe bubbles were observed within the microstructure of both HEC and HEA films (Figures B and D). The average size of these Xe bubbles was estimated to be 2.06 ± 0.3 nm and 2.12 ± 0.4 nm, respectively for the HEC and HEA films. The histograms of Xe bubbles sizes are shown in Fig. 4E and F. In addition, the estimated areal densities for both HEC and HEA films were $4.3 \pm 0.4 \times 10^{12}$ and $3.7 \pm 0.2 \times 10^{12}$ bubbles cm^{-2}, respectively. Using these areal densities, the amount of swelling in both materials was calculated to be 0.178% for the HEC and 0.18% for the HEA. Detailed information on how swelling analysis was performed is presented elsewhere [68]. For both bubble sizes and areal densities, 100 bubbles were measured in 4 different areas.

3.3.2. Morphological and microstructural modifications

A detailed track on the microstructural modifications in both HEC and HEA films is presented in the DFTEM micrographs and SAED patterns in Fig. 5. A direct comparison before and after irradiation shows that the HEC suffered small grain growth (Fig. 5A and C) whereas the HEA film exhibited significant grain growth as observed in Fig. 5E and G. The initial nanograined-equiaxed microstructure of the HEC film was preserved after irradiation, but the typical columnar-grain microstructure of the HEA appeared to exhibit recrystallization to bigger equiaxed grains. The DFTEM micrographs allowed the accurate estimation of average grain sizes. Before irradiation, the HEC and HEA films have an average grain size 9.8 ± 0.9 and 27.2 ± 2.4 nm, respectively. After irradiation, the average grain size increased to 14.9 ± 0.8 nm and 60.6 ± 4.1 nm for the HEC and HEA, respectively. In addition to the grain size analysis, the SAED patterns taken before (Fig. 5B and F) and after irradiation (Fig. 5D and H) indicate that neither the HEC nor the HEA suffered irradiation-induced amorphization.

3.3.3. Analytical quantification of the irradiation effects

A detailed investigation on possible modifications of the local alloy chemistry in both HEC and HEA films was carried out using STEM-EDX and the results are shown in Fig. 6. Elemental mapping of the HEC after annealing, but prior irradiation and after irradiation up to 10 dpa is shown in the set of Fig. 6A–F and G–M, respectively. No RIS nor RIP were detected to occur in the region corresponding to the film, but Cr segregation was observed in the AISI-316L substrate. Similarly, the elemental mapping corresponding to the HEA film before and after irradiation up to 10 dpa is shown in the set of micrographs in Fig. 6N–S and T–Y, respectively. As for the HEC film, no RIS nor RIP were detected in the HEA film. A slight Cr segregation is noted in the AISI-316L substrate. The High-Angle Annular Dark-Field (HAADF) micrographs 6AA and 6AC and the BFSTEM micrographs 6AB and 6AD shows the microstructure of the HEC and HEA films before and after irradiation corresponding to the areas where the elemental maps in the Fig. 5 were acquired. The analytical quantification of the radiation effects via STEM-EDX indicate that phase transformations, segregation or precipitation have not occurred in both materials as a result of heavy-ion irradiation.

3.4. Computational results

Formation energies of HEA in BCC and HEC in rock-salt (RS) are shown in Fig. 7A and B respectively as computed by Eq. (2). The overall

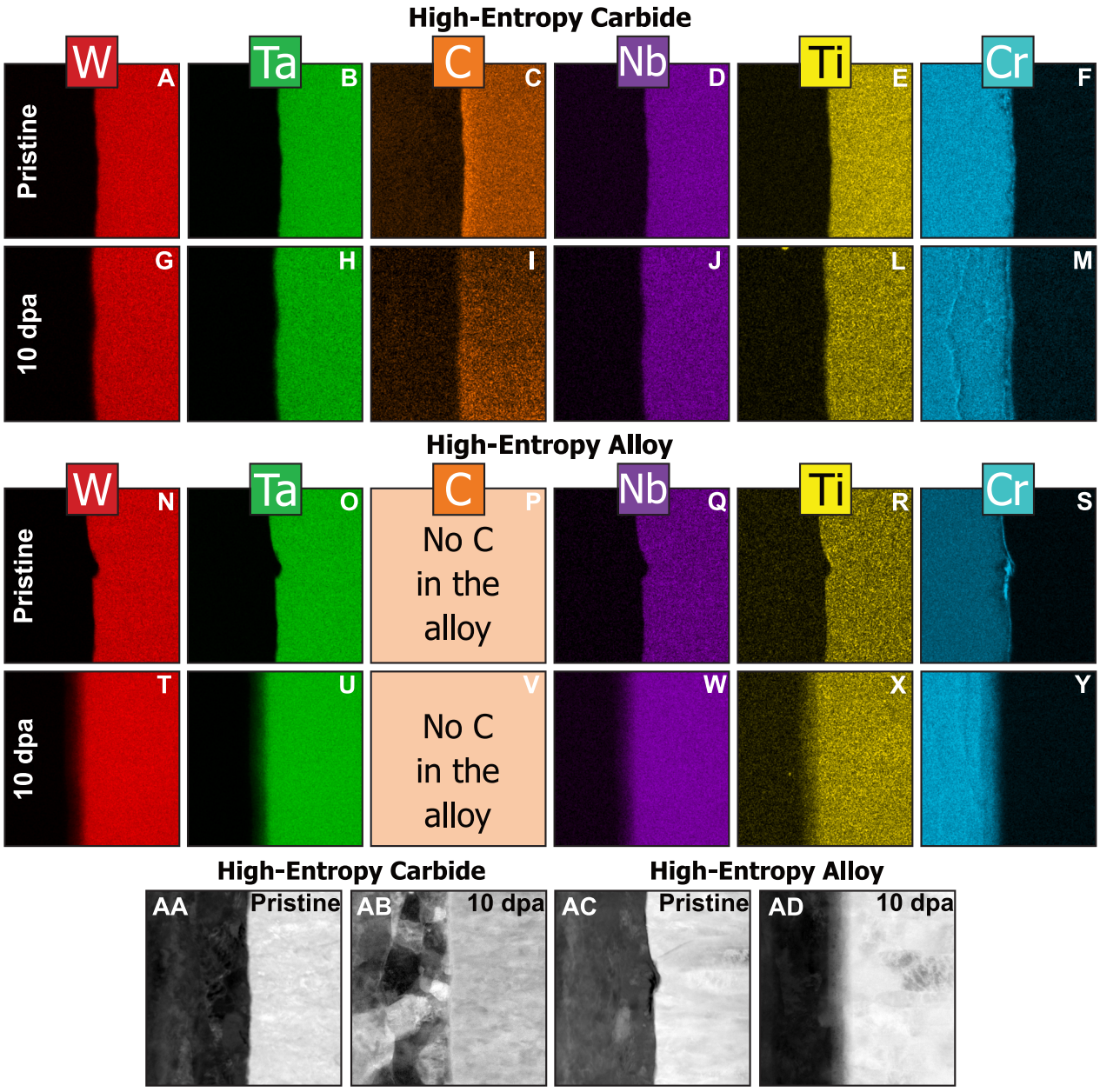

Fig. 6. Analytical microstructural investigations. The set of STEM-EDX elemental maps from A to M and from N to Y exhibit the microstructures of the HEC and HEA, respectively, before and after irradiation up to 10 dpa. The HEC and the HEA neither suffered radiation-induced segregation nor phase transformations as a result of the heavy ion irradiations. The set of HAADF and BFSTEM micrographs AA and AC, AB and AD, respectively, show the general aspect of the substrate/film system before and after irradiation. Note: the scale bar in A also applies to all micrographs in the figure.

formation energy in BCC HEA is larger than that of HEC with carbon and a RS lattice structure. The average formation energy of the HEA is -0.0238 eV per atom whilst for the HEC is -2.167 eV per atom. The deviation from the mean in the HEA is 0.00244 eV while in the HEC is 0.04376 eV. These results highlight the large stability of the carbide configuration with respect to the random metallic structure.

Formation energies of single vacancy in HEA and HEC are shown in Fig. 7C and D respectively as computed by equation 3. The mean vacancy formation energy in the HEA is larger at 3.303 eV than that in the HEC, 3.076 eV. The deviation from the mean in the HEA is 0.373 eV while the HEC has a larger deviation of 0.946 eV. The HEC has an additional set of data points stemming from the carbon atom sites which are attributed to the cation sites in the RS structure. Fig. 7E and F depicts the contribution of the mean vacancy formation energy for each atom type site. In the HEA there is a minimal difference between the mean of a Ta, 3.24 eV, and W, 3.28 eV site. In the HEC a larger discrepancy is shown between each atom type. W removal leads to a mean of 1.93 eV, while C and Ta sites have a similar mean of 3.83 eV and 3.46 eV, respectively.

4. Discussion

4.1. Characterization and comparison between the HEC and HEA counterpart

The results observed for the samples in this study are in good agreement with the findings in preceding studies, using the same synthesis conditions. Both GI-XRD and TEM analysis of the as-deposited

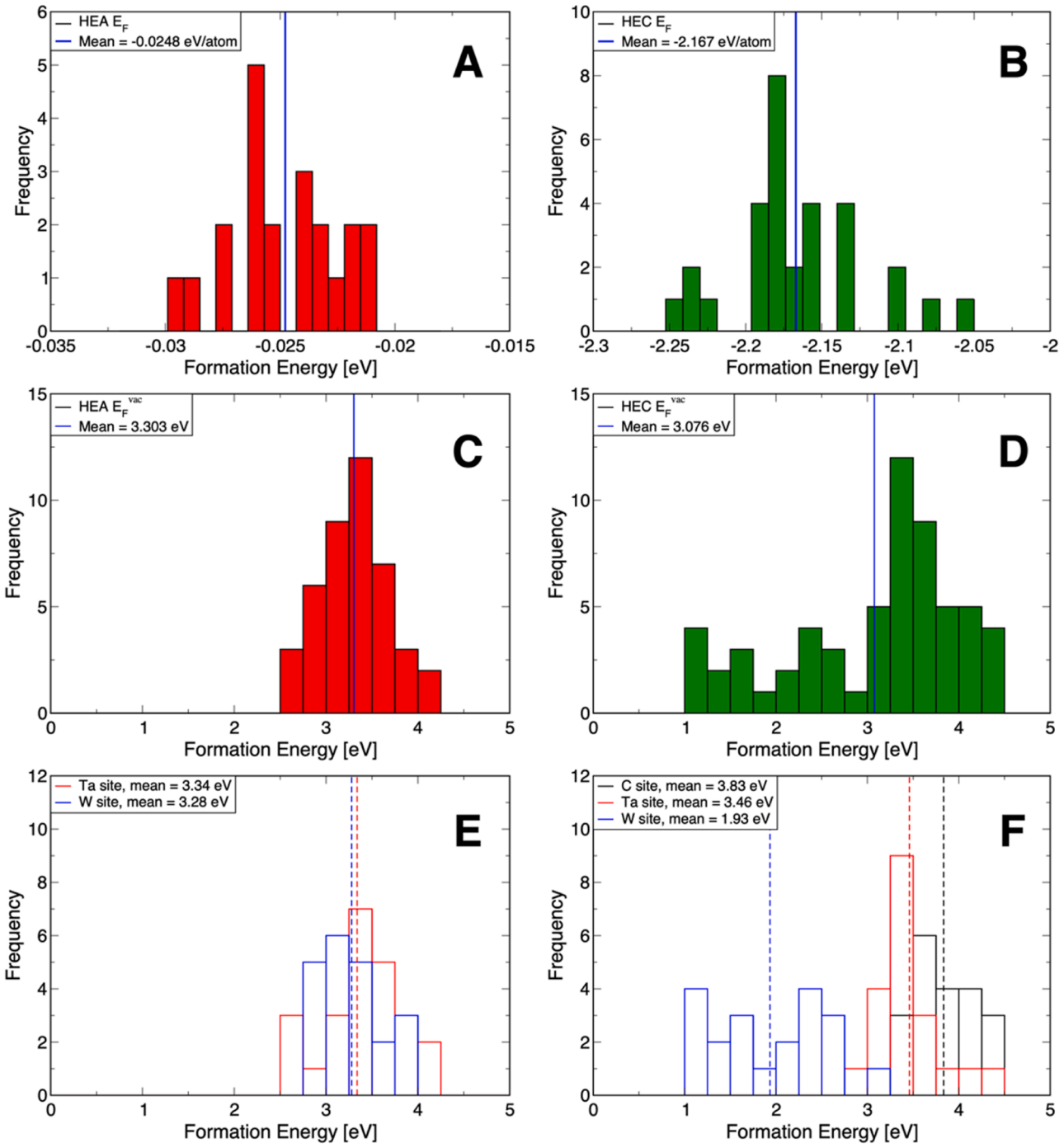

Fig. 7. Computational results. Formation energies of random configurations of HEA in BCC (A) and HEC in rock-salt (RS) (B), formation energies of single vacancy in HEA (C) and HEC (D), contribution of single vacancy on specie sites for HEA (E) and HEC (F).

coatings on steel substrates confirmed that a single-phase solid solution structure was obtained. No clustering and secondary phase formation with the metal-transition carbide formers were observed in the pristine specimens. GI-XRD measurements, with subsequent Pawley fitting analysis, confirmed the A2 (BCC) and B1-type structure for the HEA and HEC film, respectively. The fitting revealed a lattice parameter of 3.243593(117) Å for the HEA and 4.358440(354) Å for the HEC film. STEM-EDX assessment has shown no segregation of alloying elements nor secondary phases to be present in the HEC (as exhibited in Fig. 6A–F).

The feasibility of synthesizing a single-phase multicomponent alloy and carbide material in the CrNbTaTiW-C system via magnetron sputtering has been demonstrated previously [46,47,69]. The formation of a stable single-phase HEC has been attributed to the stability of the B1-type monocarbides structure for three of the five elements (Ti, Ta and Nb), as well as extensive mutual solubility of the respective monocarbides. This reasoning could possibly be expanded by an increased configurational entropy on the metal sublattice, however the effect of entropy on the phase stability of these materials is not yet clear [70].

The detailed TEM assessment of both the HEA and HEC coating showcases the differences in the microstructures of the materials, as shown in the DFTEM micrographs in Fig. 2D and E. The HEA has a characteristic columnar nanograined microstructure whereas the HEC exhibit a trend for columnar-like structure, but with the noticeable

presence of equiaxed-like nanograins. In the as-deposited state, the HEC has smaller grains when compared with the HEA. The formation of a nanocrystalline structure with smaller average grain sizes is expected for magnetron sputtered carbides, compared with metal alloys prepared under similar synthesis conditions. Carbides exhibit a higher melting point and subsequently a reduced homologous temperature (T/T_m). According to the structure zone diagram, low adatom mobility and continued re-nucleation of the grains is expected in the low homologous temperature region, resulting in the formation of a fine-grained microstructure [71,72].

4.2. Real-time radiation response of the refractory HEC and HEA counterpart

Given the differences between the CrNbTaTiW HEA and (CrNbTaTiW)C HEC in a microstructural perspective, i.e. both different crystal structures and average grain sizes, a pioneer study using heavy-ion irradiation in situ within a TEM was herein performed aiming at directly comparing the radiation effects and response of both materials in extreme conditions. As for the irradiation conditions, 300 keV Xe ions at 573 K was chosen as it provides a suitable methodology to simulate the dense displacement damage cascade conditions that are generated in structural nuclear materials and nuclear fuels due to neutrons [73,74]. Xe ions within this energy range also poses a considerable level of implantation for an electron-transparent lamella (~100 nm of thickness) and this fact was used to study Xe retention (a fission gas within the U decay chain [75]) and inert gas bubbles formation: the latter facts of paramount importance within the context of conventional ceramic-based nuclear fuels.

The microstructures of both HEC and HEA were monitored in situ within the TEM during irradiation as shown in Fig. 3A–D and E–H, respectively. From the real-time irradiation experiments, it became evident that the HEC was not subjected to the same level of grain growth as the HEA. Post-irradiation analysis using conventional TEM by comparing the irradiated microstructures at 10 dpa with pristine specimens also confirmed such observations. Both materials did not suffer amorphization as demonstrated in the SAED patterns collected before and after irradiation (Fig. 5B–D and F–H). In addition, displacement damage effects such as characteristic dislocation loops were not observed to form in these microstructures (dark contrast observed in the BFTEM micrographs in Fig. 3 is due to Bragg diffraction conditions).

As recently reviewed by Zhang et al., a characteristic property exhibited by nanocrystalline materials under irradiation is their grain boundaries (GBs) ability to actively act as preferential sinks for irradiation-induced defects at the atomic level [76]. Given the impact of heavy Xe ions within the microstructures of both materials, two particular radiation damage effects can take place: (1) the generation of a dense displacement defect cascade with a subsequent thermal spike [77] and (2) the absorption or annihilation of the lattice defects (i.e. interstitials and vacancies) generated within the cascade by the nanocrystalline GBs [78,79]. Due to such a constrained nature of GBs, it has been extensively reported that nanocrystallinity in HEAs prevents the development of dislocation loops under irradiation – with refractory and nanocrystalline HEAs being a particular case of outstanding resistance to irradiation-induced dislocation formation[46]. This fact also agrees with recent studies on plastic deformation of nanomaterials where reports show absence of dislocation emission under mechanical loading for grains with average sizes of ~10–50 nm [80]. Although, displacement damage has not been observed in both materials subjected to irradiations in this work, concerns on the radiation effects on the HEC and HEA lies solely on the morphological stability (grain growth) and possible local chemistry changes (RIS and RIP).

Classical thermal grain growth models [81] were used by Alexander-Was-Kaoumi (AWK) to formulate a modified version to empirically integrate the radiation effects [82,83]. In the AWK model, nanograins can grow upon migration caused during the generation and evolution of a displacement damage cascade. This happens as a consequence of both solid-state diffusion of defects and solutes as well as the local curvature of the grain that will point to its migration direction. The application of the AWK model to understand the mechanisms of grain growth of HEAs under irradiation has led to a conclusion that in these alloys, the irradiation-induced grain growth as a function of irradiation dose is significantly suppressed when compared with pure metals and conventional alloys [84], leading to superior radiation resistance.

The findings on the application of the AWK model to understand the radiation response of nanocrystalline HEAs agree with recent calculations presented in literature for such novel alloys. The high-radiation resistance exhibited by some refractory HEAs was recently investigated using a reaction rate model by El-Atwani et al. in the quaternary system of WTaVCr [45]. When compared with single refractory metals such as W, interstitials, and vacancies mobilities are of a closer value, which leads to a maximized recombination rate that inevitably reduces the defect population during the events of the displacement cascade. In addition to that, transition-metal carbides are of higher a melting point than its pure metal counterparts [85]. The lower grain growth levels observed for the HEC within this work is a synergistic manifestation of a smaller defect population due to irradiation – which arises as a characteristic feature on defect diffusion of high-entropy materials – as well as a higher melting point for the HEC than the HEA in this CrNbTaTiW quinary system.

4.3. Analytical evidence of enhanced local chemical stability

Heavy-ion irradiation with in situ TEM as a method to emulate [86] the dense damage cascades often observed in neutron irradiation has been revealed as a suitable methodology to investigate the radiation response of candidate nuclear materials.

Two recent literature results can be used to shed light on the radiation resistance of the materials herein investigated, especially the HEC. By using Xe irradiation within a TEM at 573 K, TiN thin films – proposed as a coating material for Accident Tolerant Fuels (ATFs) – exhibited a series of deleterious responses at only 6.2 dpa, among them RIS of Ti along its grain boundaries and Xe bubble sizes around of 30 nm [86]. Similarly, a Cr_2AlC MAX phase has shown RIS of Cr along grain boundaries around 7 dpa [87].

Despite the chemical instabilities observed in these two materials above, using similar irradiation methodology, both the HEC and HEA herein investigated have not experienced chemical instabilities such as RIS, phase transformations or amorphization. Transition metal carbides often readily undergo amorphization when irradiated with energetic particle beams, which is surprisingly not the case for the HEC. The materials sustained their initial local chemistry intact up to 10 dpa, which can be considered a high dose in the face of previous studies with potential nuclear ceramics mentioned above.

The response of both HEA and HEC to irradiation are also better understood with the computational results presented in Fig. 7. These results indicated that the potential energy landscape for the vacancy to migrate is higher in the case of the HEC compared to the HEA, with sites that may act as deep traps for vacancy diffusion. In addition, the formation energy of the HEC is lower than the HEA, suggesting a more stable thermodynamic configuration for the carbide. This variation of the defect properties has profound consequences for the response of the material upon irradiation. When the defects' energetic landscape is higher in the HEC when compared with the HEA, all the events of radiation damage will be suppressed or even "sluggish" in the carbide compared with the alloy. Similarly this happens for a more thermodynamic stable microstructure reflecting lower formation energies (the HEC case). For both facts, experimental evidence presented in this paper points to better resistance to grain growth in the case of the HEC compared with the HEA, although both materials present excellent local chemical stability despite their chemical complexity.

Table 4
Literature data on Xe bubbles sizes on post-irradiated conventional nuclear fuel ceramics and this work.

Material	Irradiation method	Xe bubble sizes (diameter/nm)	Reference
UO_2	Neutron, LWR	3-5	Cornell [97]
$(U,Pu)O_2$	Neutron, LMFBR	< 30	Matzke [91]
$(U,Pu)O_2$	Neutron, LWR	~ 6	Matzke [91]
ZrO_2 Y-stab.	Xe implantation	6	Degueldre [88]
UO_2	Xe implantation	~ 1[a]	Michel [98]
U_3Si_2	Xe implantation	5-10	Miao [99]
UC	Computational/BUCK code	0.5-2.5	Matthews [100]
(CrNbTaTiW)C	Xe implantation	2.0	This work, 2022

[a] Michel et al. reports such bubble sizes at a dose of 7×10^{14} ions cm^{-2}, one order of magnitude lower than the dose reported in this present work.

4.4. Inert gas retention and bubbles formation

A desired property for a nuclear fuel material is the ability to retain fission gases in its matrix. These gases originate from the decay chain of U stimulated by neutrons within a reactor. In the case of Xe, atoms with a kinetic energy of 182 MeV can be generated and cause damage in the reactor's material (see calculation in the supplemental file). Upon their release from the nuclear fuel matrix, an exponential increase of the nuclear fuel rod internal pressure can occur, thus the safe operational envelope of a nuclear reactor could be jeopardized. A microstructure that shows the ability to act as a physical barrier to the release of fission gases is a desire for the development of new ATFs [36,88–90].

The interaction of a highly-energetic fission gas atom with the microstructure of conventional nuclear fuels has been the subject of intense investigations over the past century and a comprehensive review including details of the physics underlying such interactions was presented by Matzke late in the 1980s with a focus on the UO_2 [91]. To briefly summarize, four types of phenomena can occur when fission gases interact with the nuclear fuel matrix in the presence of radiation damage: (i) gas entrapment in crystalline defects, (ii) precipitation into gas bubbles and/or in pre-existing pores, (iii) precipitation of the gas along the grain boundaries, and (iv) final transport of the gas atoms to the nuclear fuel rod plenum [91]. Effects (i) and (ii) are related with the retention of fission gases in the material's microstructure whereas (iii) and (iv) are linked with their release. For the purposes of innovative nuclear fuel development with high radiation tolerance, microstructural retention of fission gases is preferred [88].

Despite the high-resistance to irradiation-induced grain growth and the absence of detectable displacement damage such as dislocation loops, Xe bubbles were observed to nucleate in both HEC and HEA as a function of the irradiation dose which inserts the HEC as candidate materials for future nuclear ceramic fuels. Although the bubbles have nucleated, their growth seems to be somehow hindered as the final sizes for Xe bubbles in the HEC and HEA are, respectively, 2.06 ± 0.3 nm and 2.12 ± 0.4 nm. In addition, the amount of swelling promoted by such Xe bubbles in both materials is around 0.18% which is significantly lower than the values reported by different materials under inert gas implantations.

The high capability of fission gas retention herein exhibited by both HEC and HEA in the CrNbTaTiW refractory system can be better understood when a comparison with available literature data is made for Xe bubbles sizes in conventional nuclear fuel materials. Table 4 shows a series of Xe bubble sizes (diameter) collected from the available literature. It is notable that the bubble sizes observed for the HEC and HEA herein presented are smaller than most of the conventional nuclear ceramic fuel materials. Such a resistance to Xe bubbles growth can be understood with the state-of-the-art comprehension of high-entropy materials and the inherent nanocrystallinity. For HEAs, radiation damage production is overall reduced at the atomic level given their inherent tunable chemical disorder capability [92]. It has been reported that in some refractory HEAs, similar mobilities for vacancies and self-interstitials leads to a higher recombination rate of point defects, thus reducing the population of vacancies needed to grow large bubbles [45]. The damage cascades promoted by 300 keV Xe extend to 50 nm (according to SRIM-2013Pro calculation), thus larger than the average grain size of both HEC and HEA. Part of the defect population generated within the cascade will also annihilate in the grain boundaries, given their reduced-sizes and high sink-efficiency for atomic-size defects [93]. A similar trend has been observed in different HEA systems and in materials with grain-sizes confined at the nanoscale [45,93]. It is impressive that given such large and dense cascade of defects, only small bubbles and little grain growth are observed as major effects of the irradiation. These facts evidence the strong potential of HEC as materials for further investigations within the scope of nuclear fuels.

5. Conclusion

High-entropy materials exhibit – as shown in this paper – an enormous potential for functionalization and commercialization in the near future. A novel high-entropy carbide and its high-entropy alloy counterpart (herein defined as HEC and HEA) were investigated considering their application in extreme environments, specifically in that where energetic particle irradiation is the major degradation mechanism. The methodology of heavy ion with in situ TEM has been used for the first time to assess the irradiation response of such a novel HEC.

In face of the literature available for conventional ceramic materials under irradiation, both HEC and HEA have not displayed any local chemical instabilities (such as RIS and RIP) as a result of the atomic collisions on their microstructures. Surprisingly, amorphization did not occur for the HEC up to 10 dpa in the temperature of relevance for light-water reactors. Irradiation-induced grain growth were observed to occur in both materials with the HEC exhibiting (within the statistical error) superior performance than the HEA. Xe bubbles were observed to nucleate and grow in both materials, but their final sizes at 10 dpa were found to be much smaller than those observed for conventional nuclear fuel ceramic materials under irradiation. These results point to the HEC having a slightly higher radiation tolerance than the HEA. DFT calculations corroborate the findings presented in this paper.

By outperforming existing ceramic materials, it can be concluded that the HECs hold an enormous potential to be further investigated in the context of extreme environments. The possibility of manufacturing novel nuclear fuels materials based on the HEC concept could soon revolutionize this field by deploying new materials with enhanced radiation resistance and enhanced fission gases retention.

Data availability and request for samples

The raw data collected and used to report the results presented in this research manuscript can be found permanently stored in a dataset in the Mendeley Data repository and it can be open accessed via the link provided: https://doi.org/10.17632/scsg3dpg2y.1. We are committed to increase the efforts to evaluate the response of the high-entropy

carbides presented in this manuscript. Therefore, samples can reasonably be provided for the community upon request to Dr. Stefan Fritze (ist.stefanf@gmail.com), MSc. Barbara Osinger (barbara.osinger@kemi.uu.se) or Professor Ulf Jansson (ulf.jansson@kemi.uu.se).

Declaration of Competing Interest

The authors declare that they have no known competing financial interests or personal relationships that could have appeared to influence the work reported in this paper.

Acknowledgments

Funding for this research has been primarily provided by the European Research Council excellence science grant "TRANSDESIGN" under contract number 757961. The research presented in this article was supported by the Laboratory Directed Research and Development program established at the Los Alamos National Laboratory under the project numbers 20200689PRD2 and 20200511ECR. All the authors are grateful for the support provided by the MIAMI facilities at the University of Huddersfield by means of funding from the Engineering and Physical sciences Research Council (EPSRC) under the grants EP/E017266/1 and EP/M028283/1. The Austrian Research Promotion Agency (FFG) support in the project 3DnanoAnalytics (FFG-No. 858040) is also greatly appreciated. Infrastructural grants by VR-RFI [grant numbers 2017-00646_9, 2019_00191]; and SSF [contract RIF14-0053] supporting accelerator operation are gratefully acknowledged. Lars Riekehr is also acknowledged for his support with FIB and TEM at Uppsala University. MAT would like to thank Professor Yanwen Zhang (UTK/ORNL) for previous discussions regarding the results herein presented.

Supplementary materials

Supplementary material associated with this article can be found, in the online version, at doi:10.1016/j.actamat.2023.118856.

References

[1] B. Cantor, I.T.H.T.H. Chang, P. Knight, A.J.B.J.B. Vincent, Microstructural development in equiatomic multicomponent alloys, Mater. Sci. Eng. 375–377 (2004) 213–218, https://doi.org/10.1016/j.msea.2003.10.257.
[2] J.-W. Yeh, Physical metallurgy of high-entropy alloys, JOM 67 (2015) 2254–2261, https://doi.org/10.1007/s11837-015-1583-5.
[3] B.S. Murty, J.W. Yeh, S. Ranganathan, High-Entropy Alloys, Butterworth-Heinemann, 2014, https://doi.org/10.1016/B978-0-12-800251-3.00002-X.
[4] J.-W. Yeh, S.-K. Chen, S.-J. Lin, J.-Y. Gan, T.-S. Chin, T.-T. Shun, C.-H. Tsau, S.-Y. Chang, Nanostructured high-entropy alloys with multiple principal elements: novel alloy design concepts and outcomes, Adv. Eng. Mater. 6 (2004) 299–303, https://doi.org/10.1002/adem.200300567.
[5] B. Cantor, Stable and metastable multicomponent alloys, Ann. Chim. Sci. Matér. 32 (2007) 245–256, https://doi.org/10.3166/acsm.32.245-256.
[6] B. Cantor, K.B. Kim, P.J. Warren, Novel multicomponent amorphous alloys, Mater. Sci. Forum 386–388 (2002) 27–32, https://doi.org/10.4028/www.scientific.net/MSF.386-388.27.
[7] M.-H. Tsai, J.-W. Yeh, High-entropy alloys: a critical review, Mater. Res. Lett. 2 (2014) 107–123, https://doi.org/10.1080/21663831.2014.912690.
[8] Y.F.F. Ye, Q. Wang, J. Lu, C.T.T. Liu, Y. Yang, High-entropy alloy: challenges and prospects, Mater. Today 19 (2016) 349–362, https://doi.org/10.1016/j.mattod.2015.11.026.
[9] Y.E.H. Jien-Wei, Recent progress in high-entropy alloys, Ann. Chim. Sci. Mater. 31 (2006) 633–648.
[10] C.G. Schön, T. Duong, Y. Wang, R. Arróyave, Probing the entropy hypothesis in highly concentrated alloys, Acta Mater. 148 (2018) 263–279, https://doi.org/10.1016/j.actamat.2018.01.028.
[11] C.G. Schön, T. Duong, Y. Wang, R. Arróyave, A proof of concept: thermodynamics of aluminum – transition metal highly concentrated alloys, J. Alloys Compd. 781 (2019) 595–605, https://doi.org/10.1016/j.jallcom.2018.12.068.
[12] C.G. Schön, M.A. Tunes, R. Arróyave, J. Ågren, On the complexity of solid-state diffusion in highly concentrated alloys and the sluggish diffusion core-effect, Calphad 68 (2020), 101713, https://doi.org/10.1016/j.calphad.2019.101713.
[13] M.A. Tunes, H. Le, G. Greaves, C.G. Schön, H. Bei, Y. Zhang, P.D. Edmondson, S. E. Donnelly, Investigating sluggish diffusion in a concentrated solid solution alloy using ion irradiation with in situ TEM, Intermetallics (Barking) 110 (2019), 106461, https://doi.org/10.1016/j.intermet.2019.04.004.
[14] A. Paul, Comments on "Sluggish diffusion in Co–Cr–Fe–Mn–Ni high-entropy alloys" by K.Y. Tsai, M.H. Tsai and J.W. Yeh, Acta Materialia 61 (2013) 4887–4897, Scr. Mater. 135 (2017) 153–157, https://doi.org/10.1016/j.scriptamat.2017.03.026.
[15] F. Otto, Y. Yang, H. Bei, E.P. George, Relative effects of enthalpy and entropy on the phase stability of equiatomic high-entropy alloys, Acta Mater. 61 (2013) 2628–2638, https://doi.org/10.1016/J.ACTAMAT.2013.01.042.
[16] M.S. Daw, M. Chandross, Sluggish diffusion in random equimolar FCC alloys, Phys. Rev. Mater. 5 (2021), 043603, https://doi.org/10.1103/physrevmaterials.5.043603.
[17] H.K.D.H. Bhadeshia, High entropy alloys, Mater. Sci. Technol. 31 (2015) 1139–1141, https://doi.org/10.1179/0267083615Z.000000000969.
[18] A. Fernández-Caballero, J.S. Wróbel, P.M. Mummery, D. Nguyen-Manh, Short-range order in high entropy alloys: theoretical formulation and application to Mo–Nb–Ta–V–W system, J. Phase Equilib. Diffus. 38 (2017) 391–403, https://doi.org/10.1007/s11669-017-0582-3.
[19] Y. Shi, B. Yang, P. Liaw, Corrosion-resistant high-entropy alloys: a review, Metals (Basel). 7 (2017) 43, https://doi.org/10.3390/met7020043.
[20] W.J. Weber, Y. Zhang, Predicting damage production in monoatomic and multi-elemental targets using stopping and range of ions in matter code: challenges and recommendations, Curr. Opin. Solid State Mater. Sci. 23 (2019), 100757, https://doi.org/10.1016/j.cossms.2019.06.001.
[21] S. Zhao, Y. Osetsky, Y. Zhang, Preferential diffusion in concentrated solid solution alloys: NiFe, NiCo and NiCoCr, Acta Mater. 128 (2017) 391–399, https://doi.org/10.1016/j.actamat.2017.01.056.
[22] M.W. Ullah, D.S. Aidhy, Y. Zhang, W.J. Weber, Damage accumulation in ion-irradiated Ni-based concentrated solid-solution alloys, Acta Mater. 109 (2016), https://doi.org/10.1016/j.actamat.2016.02.048.
[23] F. Zhang, Y. Tong, K. Jin, H. Bei, W.J. Weber, A. Huq, A. Lanzirotti, M. Newville, D.C. Pagan, J.Y.P. Ko, Y. Zhang, Chemical complexity induced local structural distortion in NiCoFeMnCr high-entropy alloy, Mater. Res. Lett. 6 (2018) 450–455, https://doi.org/10.1080/21663831.2018.1478332.
[24] Y. Zhang, M.A. Tunes, M.L. Crespillo, F. Zhang, W.L. Boldman, P.D. Rack, L. Jiang, C. Xu, G. Greaves, S.E. Donnelly, L. Wang, W.J. Weber, Thermal stability and irradiation response of nanocrystalline CoCrCuFeNi high-entropy alloy, Nanotechnology 30 (2019), 294004, https://doi.org/10.1088/1361-6528/ab1605.
[25] C. Lu, T. Yang, K. Jin, G. Velisa, P. Xiu, M. Song, Q. Peng, F. Gao, Y. Zhang, H. Bei, W.J. Weber, L. Wang, Enhanced void swelling in NiCoFeCrPd high-entropy alloy by indentation-induced dislocations, Mater. Res. Lett. 6 (2018) 584–591, https://doi.org/10.1080/21663831.2018.1504136.
[26] L. Jiang, Y.-J. Hu, K. Sun, P. Xiu, M. Song, Y. Zhang, W.L. Boldman, M. L. Crespillo, P.D. Rack, L. Qi, et al., Irradiation-induced extremes create hierarchical face-/body-centered-cubic phases in nanostructured high entropy alloys, Adv. Mater. 32 (2020), 2002652.
[27] C. Lu, L. Niu, N. Chen, K. Jin, T. Yang, P. Xiu, Y. Zhang, F. Gao, H. Bei, S. Shi, M.-R. He, I.M. Robertson, W.J. Weber, L. Wang, Enhancing radiation tolerance by controlling defect mobility and migration pathways in multicomponent single-phase alloys, Nat. Commun. 7 (2016) 13564, https://doi.org/10.1038/ncomms13564.
[28] Y. Zhang, G.M. Stocks, K. Jin, C. Lu, H. Bei, B.C. Sales, L. Wang, L.K. Béland, R. E. Stoller, G.D. Samolyuk, M. Caro, A. Caro, W.J. Weber, Influence of chemical disorder on energy dissipation and defect evolution in concentrated solid solution alloys, Nat. Commun. 6 (2015) 8736, https://doi.org/10.1038/ncomms9736.
[29] Y. Zhang, K. Jin, H. Xue, C. Lu, R.J. Olsen, L.K. Beland, M.W. Ullah, S. Zhao, H. Bei, D.S. Aidhy, G.D. Samolyuk, L. Wang, M. Caro, A. Caro, G.M. Stocks, B. C. Larson, I.M. Robertson, A.A. Correa, W.J. Weber, Influence of chemical disorder on energy dissipation and defect evolution in advanced alloys, J. Mater. Res. 31 (2016) 2363–2375, https://doi.org/10.1557/jmr.2016.269.
[30] E.J. Pickering, A.W. Carruthers, P.J. Barron, S.C. Middleburgh, D.E.J. Armstrong, A.S. Gandy, High-entropy alloys for advanced nuclear applications, Entropy (2021) 98, https://doi.org/10.3390/E23010098, 23.
[31] Y. Zhang, C. Silva, T.G. Lach, M.A. Tunes, Y. Zhou, L. Nuckols, W.L. Boldman, P. D. Rack, S.E. Donnelly, L. Jiang, L. Wang, W.J. Weber, Role of electronic energy loss on defect production and interface stability: comparison between ceramic materials and high-entropy alloys, Curr. Opin. Solid State Mater. Sci. 26 (2022), 101001, https://doi.org/10.1016/J.COSSMS.2022.101001.
[32] M.A. Tunes, L. Stemper, G. Greaves, P.J. Uggowitzer, S. Pogatscher, Prototypic lightweight alloy design for stellar-radiation environments, Adv. Sci. 7 (2020), 2002397, https://doi.org/10.1002/advs.202002397.
[33] S.J. Zinkle, G.S. Was, Materials challenges in nuclear energy, Acta Mater. 61 (2013) 735–758, https://doi.org/10.1016/j.actamat.2012.11.004.
[34] P. Yvon, F. Carré, Structural materials challenges for advanced reactor systems, J. Nucl. Mater. 385 (2009) 217–222, https://doi.org/10.1016/j.jnucmat.2008.11.026.
[35] K.L. Murty, I. Charit, Structural materials for Gen-IV nuclear reactors: challenges and opportunities, J. Nucl. Mater. 383 (2008) 189–195, https://doi.org/10.1016/j.jnucmat.2008.08.044.
[36] K.A. Terrani, Accident tolerant fuel cladding development: promise, status, and challenges, J. Nucl. Mater. 501 (2018) 13–30, https://doi.org/10.1016/j.jnucmat.2017.12.043.
[37] J.A. Aguiar, A.M. Jokisaari, M. Kerr, R.Allen Roach, Bringing nuclear materials discovery and qualification into the 21st century, Nat. Commun. 11 (2020) 2556, https://doi.org/10.1038/s41467-020-16406-2.

[38] U. Jansson, E. Lewin, Sputter deposition of transition-metal carbide films—A critical review from a chemical perspective, Thin Solid Films 536 (2013) 1–24, https://doi.org/10.1016/j.tsf.2013.02.019.

[39] P. Sarker, T. Harrington, C. Toher, C. Oses, M. Samiee, J.P. Maria, D.W. Brenner, K.S. Vecchio, S. Curtarolo, High-entropy high-hardness metal carbides discovered by entropy descriptors, Nat. Commun. 9 (1) (2018) 1–10, https://doi.org/10.1038/s41467-018-07160-7.

[40] A. Calzolari, C. Oses, C. Toher, M. Esters, X. Campilongo, S.P. Stepanoff, D. E. Wolfe, S. Curtarolo, Plasmonic high-entropy carbides, Nat. Commun. 13 (1) (2022) 1–9, https://doi.org/10.1038/s41467-022-33497-1.

[41] T.J. Harrington, J. Gild, P. Sarker, C. Toher, C.M. Rost, O.F. Dippo, C. McElfresh, K. Kaufmann, E. Marin, L. Borowski, P.E. Hopkins, J. Luo, S. Curtarolo, D. W. Brenner, K.S. Vecchio, Phase stability and mechanical properties of novel high entropy transition metal carbides, Acta Mater. 166 (2019) 271–280, https://doi.org/10.1016/J.ACTAMAT.2018.12.054.

[42] F. Wang, X. Yan, T. Wang, Y. Wu, L. Shao, M. Nastasi, Y. Lu, B. Cui, Irradiation damage in (Zr0.25Ta0.25Nb0.25Ti0.25)C high-entropy carbide ceramics, Acta Mater. 195 (2020) 739–749, https://doi.org/10.1016/J.ACTAMAT.2020.06.011.

[43] Y. Zhu, J. Chai, Z. Wang, T. Shen, L. Niu, S. Li, P. Jin, H. Zhang, J. Li, M. Cui, Microstructural damage evolution of (WTiVNbTa)C5 high-entropy carbide ceramics induced by self-ions irradiation, J. Eur. Ceram. Soc. 42 (2022) 2567–2576, https://doi.org/10.1016/J.JEURCERAMSOC.2022.01.061.

[44] B.S. Murty, J.-W. Yeh, S. Ranganathan, High-Entropy Alloys, Butterworth-Heinemann, 2014.

[45] O. El-Atwani, N. Li, M. Li, A. Devaraj, J.K.S. Baldwin, M.M. Schneider, D. Sobieraj, J.S. Wróbel, D. Nguyen-Manh, S.A. Maloy, E. Martinez, Outstanding radiation resistance of tungsten-based high-entropy alloys, Sci. Adv. 5 (2019) eaav2002, https://doi.org/10.1126/sciadv.aav2002.

[46] P. Malinovskis, S. Fritze, L. Riekehr, L. von Fieandt, J. Cedervall, D. Rehnlund, L. Nyholm, E. Lewin, U. Jansson, Synthesis and characterization of multicomponent (CrNbTaTiW)C films for increased hardness and corrosion resistance, Mater. Des. 149 (2018) 51–62, https://doi.org/10.1016/j.matdes.2018.03.068.

[47] S. Fritze, P. Malinovskis, L. Riekehr, L. von Fieandt, E. Lewin, U. Jansson, Hard and crack resistant carbon supersaturated refractory nanostructured multicomponent coatings, Sci. Rep. 8 (2018) 1–8, https://doi.org/10.1038/s41598-018-32932-y.

[48] J.A. Leavitt, L.C. McIntyre, P. Stoss, J.G. Oder, M.D. Ashbaugh, B. Dezfouly-Arjomandy, Z.M. Yang, Z. Lin, Cross sections for 170.5° backscattering of 4He from carbon for 4He energies between 1.6 and 5.0 MeV, Nucl. Instrum. Methods Phys. Res. B 40–41 (1989), https://doi.org/10.1016/0168-583X(89)90476-X.

[49] A.F. Gurbich, SigmaCalc recent development and present status of the evaluated cross-sections for IBA, Nucl. Instrum. Methods Phys. Res. B 371 (2016) 27–32, https://doi.org/10.1016/J.NIMB.2015.09.035.

[50] S.A. Corrêa, E. Pitthan, M.v. Moro, D. Primetzhofer, A multipurpose set-up using keV ions for nuclear reaction analysis, high-resolution backscattering spectrometry, low-energy PIXE and in-situ irradiation experiments, Nucl. Instrum. Methods Phys. Res. B 478 (2020) 104–110, https://doi.org/10.1016/J.NIMB.2020.05.023.

[51] J.L. Campbell, N.I. Boyd, N. Grassi, P. Bonnick, J.A. Maxwell, The Guelph PIXE software package IV, Nucl. Instrum. Methods Phys. Res. B 268 (2010), https://doi.org/10.1016/j.nimb.2010.07.012.

[52] P. Ström, P. Petersson, M. Rubel, G. Possnert, A combined segmented anode gas ionization chamber and time-of-flight detector for heavy ion elastic recoil detection analysis, Rev. Sci. Instrum. 87 (2016), 103303, https://doi.org/10.1063/1.4963709.

[53] K. Arstila, J. Julin, M.I. Laitinen, J. Aalto, T. Konu, S. Kärkkäinen, S. Rahkonen, M. Raunio, J. Itkonen, J.P. Santanen, T. Tuovinen, T. Sajavaara, Potku—New analysis software for heavy ion elastic recoil detection analysis, Nucl. Instrum. Methods Phys. Res. B 331 (2014) 34–41, https://doi.org/10.1016/J.NIMB.2014.02.016.

[54] A.A. Coelho, TOPAS and TOPAS-academic : an optimization program integrating computer algebra and crystallographic objects written in C++, J. Appl. Crystallogr. 51 (2018) 210–218, https://doi.org/10.1107/S1600576718000183.

[55] A.A. Coelho, J. Evans, I. Evans, A. Kern, S. Parsons, The TOPAS symbolic computation system, Powder Diffr. 26 (2011) S22–S25, https://doi.org/10.1154/1.3661087.

[56] J. Mayer, L.A. Giannuzzi, T. Kamino, J. Michael, TEM sample preparation and FIB-induced damage, MRS Bull. 32 (2007) 400–407, https://doi.org/10.1557/mrs2007.63.

[57] C.A. Schneider, W.S. Rasband, K.W. Eliceiri, NIH Image to ImageJ: 25 years of image analysis, Nat. Methods 9 (2012) 671–675, https://doi.org/10.1038/nmeth.2089.

[58] G. Greaves, A.H. Mir, R.W. Harrison, M.A. Tunes, S.E. Donnelly, J.A. Hinks, New microscope and ion accelerators for materials investigations (MIAMI-2) system at the University of Huddersfield, Nucl. Instrum. Methods Phys. Res. A 931 (2019) 37–43, https://doi.org/10.1016/j.nima.2019.03.074.

[59] R.E. Stoller, M.B. Toloczko, G.S. Was, A.G. Certain, S. Dwaraknath, F.A. Garner, On the use of SRIM for computing radiation damage exposure, Nucl. Instrum. Methods Phys. Res. B 310 (2013) 75–80, https://doi.org/10.1016/j.nimb.2013.05.008.

[60] ASTM International, Standard practice for neutron radiation damage simulation by charged-particle. Annual Book of ASTM Standards, 2009, pp. 1–21, https://doi.org/10.1520/E0521-96R09E01.

[61] G. Kresse, J. Hafner, Ab initio molecular dynamics for liquid metals, Phys. Rev. B 47 (1993) 558–561, https://doi.org/10.1103/PhysRevB.47.558.

[62] G. Kresse, J. Furthmüller, Efficient iterative schemes for ab initio total-energy calculations using a plane-wave basis set, Phys. Rev. B 54 (1996) 11169–11186, https://doi.org/10.1103/PhysRevB.54.11169.

[63] J.P. Perdew, K. Burke, M. Ernzerhof, Generalized gradient approximation made simple, Phys. Rev. Lett. 77 (1996) 3865–3868, https://doi.org/10.1103/PhysRevLett.77.3865.

[64] H.J. Monkhorst, J.D. Pack, Special points for Brillouin-zone integrations, Phys. Rev. B 13 (1976) 5188–5192, https://doi.org/10.1103/PhysRevB.13.5188.

[65] J.M.C. Miscione, F.C. da Silva, M.L. Marcondes, H.M. Petrilli, C.G. Schön, Evaluating residual stresses in compositionally graded TiN films via ab initio and Rietveld simulation, Materialia (Oxf). 28 (2023), 101715, https://doi.org/10.1016/J.MTLA.2023.101715.

[66] L. Casillas-Trujillo, B. Osinger, R. Lindblad, D. Karlsson, A.I. Abrikosov, S. Fritze, K. Von Fieandt, B. Alling, I. Hotz, U. Jansson, I.A. Abrikosov, E. Lewin, Experimental and theoretical evidence of charge transfer in multi-component alloys – how chemical interactions reduce atomic size mismatch, Mater. Chem. Front. 5 (2021) 5746–5759, https://doi.org/10.1039/D1QM00380A.

[67] B. Osinger, H. Mao, S. Fritze, L. Riekehr, U. Jansson, E. Lewin, Investigation of the phase formation in magnetron sputtered hard multicomponent (HfNbTiVZr)C coatings, Mater. Des. 221 (2022), 111002, https://doi.org/10.1016/J.MATDES.2022.111002.

[68] O. El-Atwani, J.A. Hinks, G. Greaves, J.P. Allain, S.A. Maloy, Grain size threshold for enhanced irradiation resistance in nanocrystalline and ultrafine tungsten, Mater. Res. Lett. 5 (2017) 343–349, https://doi.org/10.1080/21663831.2017.1292326.

[69] D. Shinde, S. Fritze, M. Thuvander, P. Malinovskis, L. Riekehr, U. Jansson, K. Stiller, Elemental distribution in CrNbTaTiW-C high entropy alloy thin films, Microsc. Microanal. 25 (2019) 489–500, https://doi.org/10.1017/S1431927618016264.

[70] J.M. Schneider, How high is the entropy in high entropy ceramics? J. Appl. Phys. 130 (2021), 150903 https://doi.org/10.1063/5.0062523.

[71] J.A. Thornton, The microstructure of sputter-deposited coatings, J. Vac. Sci. Technol. A 4 (1986) 3059–3065.

[72] A. Anders, A structure zone diagram including plasma-based deposition and ion etching, Thin Solid Films 518 (2010) 4087–4090, https://doi.org/10.1016/J.TSF.2009.10.145.

[73] C.A. English, B.L. Eyre, Heavy-ion damage in alpha-Fe, Nature 260 (1976) 619–621, https://doi.org/10.1038/260170a0.

[74] C.A. English, Low-dose neutron irradiation damage in FCC and BCC metals, J. Nucl. Mater. 108–109 (1982) 104–123, https://doi.org/10.1016/0022-3115(82)90477-9.

[75] Y.-S. Youn, S.D. Park, J.-Y. Kim, J.-Y. Park, Y.-K. Ha, Quantitative and isotopic analysis of released and retained krypton and xenon fission gases from irradiated metallic fuels, J. Radioanal. Nucl. Chem. 312 (2017) 517–521, https://doi.org/10.1007/s10967-017-5254-6.

[76] X. Zhang, K. Hattar, Y. Chen, L. Shao, J. Li, C. Sun, K. Yu, N. Li, M.L. Taheri, H. Wang, J. Wang, M. Nastasi, Radiation damage in nanostructured materials, Prog. Mater. Sci. 96 (2018) 217–321, https://doi.org/10.1016/j.pmatsci.2018.03.002.

[77] J.A. Brinkman, On the nature of radiation damage in metals, J. Appl. Phys. 25 (1954) 961–970, https://doi.org/10.1063/1.1721810.

[78] R. Bullough, M.R. Hayns, M.H. Wood, Sink strengths for thin film surfaces and grain boundaries, J. Nucl. Mater. 90 (1980) 44–59, https://doi.org/10.1016/0022-3115(80)90244-5.

[79] A.D. Brailsford, R. Bullough, M.R. Hayns, Point defect sink strengths and void-swelling, J. Nucl. Mater. 60 (1976) 246–256.

[80] H. Conrad, J. Narayan, Mechanisms governing the plastic deformation of nanocrystalline materials, including grain-size softening, Mechanical Properties of Nanocrystalline Materials (2011) 1–29, https://doi.org/10.1201/b11164-2.

[81] J.E. Burke, D. Turnbull, Recrystallization and grain growth, Prog. Metal Phys. 3 (1952) 220–292, https://doi.org/10.1016/0502-8205(52)90009-9.

[82] D.E. Alexander, G.S. Was, Thermal-spike treatment of ion-induced grain growth: theory and experimental comparison, Phys. Rev. B 47 (1993) 2983–2994, https://doi.org/10.1103/PhysRevB.47.2983.

[83] D. Kaoumi, A.T. Motta, R.C. Birtcher, A thermal spike model of grain growth under irradiation, J. Appl. Phys. 104 (2008).

[84] M.A. Tunes, G. Greaves, P.D. Rack, W.L. Boldman, C.G. Schön, S. Pogatscher, S. A. Maloy, Y. Zhang, O. El-Atwani, Irradiation stability and induced ferromagnetism in a nanocrystalline CoCrCuFeNi highly-concentrated alloy, Nanoscale 13 (2021) 20437–20450, https://doi.org/10.1039/D1NR04915A.

[85] P. Sarker, T. Harrington, C. Toher, C. Oses, M. Samiee, J.P. Maria, D.W. Brenner, K.S. Vecchio, S. Curtarolo, High-entropy high-hardness metal carbides discovered by entropy descriptors, Nat. Commun. 9 (2018) 4980, https://doi.org/10.1038/s41467-018-07160-7.

[86] M.A. Tunes, F.C. da Silva, O. Camara, C.G. Schön, J.C. Sagás, L.C. Fontana, S. E. Donnelly, G. Greaves, P.D. Edmondson, Energetic particle irradiation study of TiN coatings: are these films appropriate for accident tolerant fuels? J. Nucl. Mater. 512 (2018) 239–245, https://doi.org/10.1016/j.jnucmat.2018.10.013.

[87] M.A. Tunes, M. Imtyazuddin, C. Kainz, S. Pogatscher, V.M. Vishnyakov, Deviating from the pure MAX phase concept: radiation-tolerant nanostructured dual-phase Cr_2AlC, Sci. Adv. 7 (2021) 6771–6795, https://doi.org/10.1126/SCIADV.ABF6771.

[88] C. Degueldre, M. Pouchon, M. Döbeli, K. Sickafus, K. Hojou, G. Ledergerber, S. Abolhassani-Dadras, Behaviour of implanted xenon in yttria-stabilised zirconia as inert matrix of a nuclear fuel, J. Nucl. Mater. 289 (2001) 115–121, https://doi.org/10.1016/S0022-3115(00)00690-5.

[89] Shannon Bragg-Sitton, Development of advanced accident-tolerant fules for commercial LWRs, Nucl. News (2014) 83–91.
[90] S.J. Zinkle, K.A. Terrani, J.C. Gehin, L.J. Ott, L.L. Snead, Accident tolerant fuels for LWRs: a perspective, J. Nucl. Mater. 448 (2014) 374–379, https://doi.org/10.1016/j.jnucmat.2013.12.005.
[91] H.J. Matzke, Gas release mechanisms in UO_2—a critical review, Radiat. Eff. 53 (1980) 219–242, https://doi.org/10.1080/00337578008207118.
[92] Y. Zhang, Y.N. Osetsky, W.J. Weber, Tunable chemical disorder in concentrated alloys: defect physics and radiation performance, Chem. Rev. (2021), https://doi.org/10.1021/ACS.CHEMREV.1C00387 acs.chemrev.1c00387.
[93] E. Aradi, M.A. Tunes, J. Lewis-Fell, G. Greaves, H. Antrekowitsch, S. Pogatscher, S.E. Donnelly, J.A. Hinks, Radiation damage suppression in AISI-316 steel nanoparticles: implications for the design of future nuclear materials, ACS Appl. Nano Mater. 3 (2020) 9652–9662, https://doi.org/10.1021/acsanm.0c01611.
[94] M. Mayer, SIMNRA, a simulation program for the analysis of NRA, RBS and ERDA, in: AIP Conf. Proc., AIP, 1999, https://doi.org/10.1063/1.59188.
[95] K. Nakamura, M. Yashima, Crystal structure of NaCl-type transition metal monocarbides MC (M = V, Ti, Nb, Ta, Hf, Zr), a neutron powder diffraction study, Mater. Sci. Eng. 148 (2008) 69–72, https://doi.org/10.1016/J.MSEB.2007.09.040.
[96] D. Huang, S. Liu, H. Xu, Y. Du, Phase equilibria of the Mg–Mn–Zn system at 593 K (320 °C), J. Alloys Compd. 688 (2016) 1115–1124, https://doi.org/10.1016/J.JALLCOM.2016.07.120.
[97] R.M. Cornell, An electron microscope examination of matrix fission-gas bubbles in irradiated uranium dioxide, J. Nucl. Mater. 38 (1971) 319–328, https://doi.org/10.1016/0022-3115(71)90061-4.
[98] A. Michel, C. Sabathier, G. Carlot, O. Kaïtasov, S. Bouffard, P. Garcia, C. Valot, An in situ TEM study of the evolution of Xe bubble populations in UO_2, Nucl. Instrum. Methods Phys. Res. B 272 (2012) 218–221, https://doi.org/10.1016/j.nimb.2011.01.069.
[99] Y. Miao, J. Harp, K. Mo, S. Zhu, T. Yao, J. Lian, A.M. Yacout, Bubble morphology in U3Si2 implanted by high-energy Xe ions at 300 °C, Journal of Nuclear Materials 495 (2017) 146–153, https://doi.org/10.1016/j.jnucmat.2017.07.066.
[100] C. Matthews, Fission Gas Bubble Behavior in Uranium Carbide, Oregon State University, 2015. https://ir.library.oregonstate.edu/concern/graduate_thesis_or_dissertations/p8418r053?locale=en (accessed October 24, 2021).